

This is an electronic reprint of the original article. This reprint may differ from the original in pagination and typographic detail.

CeFeO₃-CeO₂-Fe₂O₃ Systems

Matveyeva, Anna N.; Omarov, Shamil O.; Gavrilova, Marianna A.; Sladkovskiy, Dmitry A.; Murzin, Dmitry Yu

Published in:
Materials

DOI:
[10.3390/ma15227970](https://doi.org/10.3390/ma15227970)

Published: 01/11/2022

Document Version
Final published version

Document License
CC BY

[Link to publication](#)

Please cite the original version:

Matveyeva, A. N., Omarov, S. O., Gavrilova, M. A., Sladkovskiy, D. A., & Murzin, D. Y. (2022). CeFeO₃-CeO₂-Fe₂O₃ Systems: Synthesis by Solution Combustion Method and Catalytic Performance in CO₂ Hydrogenation. *Materials*, 15(22), Article 7970. <https://doi.org/10.3390/ma15227970>

General rights

Copyright and moral rights for the publications made accessible in the public portal are retained by the authors and/or other copyright owners and it is a condition of accessing publications that users recognise and abide by the legal requirements associated with these rights.

Take down policy

If you believe that this document breaches copyright please contact us providing details, and we will remove access to the work immediately and investigate your claim.

Article

CeFeO₃–CeO₂–Fe₂O₃ Systems: Synthesis by Solution Combustion Method and Catalytic Performance in CO₂ Hydrogenation

Anna N. Matveyeva ¹, Shamil O. Omarov ¹, Marianna A. Gavrilova ^{1,2}, Dmitry A. Sladkovskiy ² and Dmitry Yu. Murzin ^{3,*}

¹ Laboratory of Materials and Processes for Hydrogen Energy, Ioffe Institute, Politeknicheskaya ul. 28, 194021 St. Petersburg, Russia

² Resource-Saving Department, St. Petersburg State Institute of Technology (Technical University), Moskovskiy pr. 26, 190013 St. Petersburg, Russia

³ Laboratory of Industrial Chemistry and Reaction Engineering, Åbo Akademi University, Henriksgatan 2, 20500 Turku, Finland

* Correspondence: dmurzin@abo.fi

Abstract: Rare-earth orthoferrites have found wide application in thermocatalytic reduction-oxidation processes. Much less attention has been paid, however, to the production of CeFeO₃, as well as to the study of its physicochemical and catalytic properties, in particular, in the promising process of CO₂ utilization by hydrogenation to CO and hydrocarbons. This study presents the results of a study on the synthesis of CeFeO₃ by solution combustion synthesis (SCS) using various fuels, fuel-to-oxidizer ratios, and additives. The SCS products were characterized by XRD, FTIR, N₂-physisorption, SEM, DTA–TGA, and H₂-TPR. It has been established that glycine provides the best yield of CeFeO₃, while the addition of NH₄NO₃ promotes an increase in the amount of CeFeO₃ by 7–12 wt%. In addition, the synthesis of CeFeO₃ with the participation of NH₄NO₃ makes it possible to surpass the activity of the CeO₂–Fe₂O₃ system at low temperatures (300–400 °C), as well as to increase selectivity to hydrocarbons. The observed effects are due to the increased gas evolution and ejection of reactive FeO_x nanoparticles on the surface of crystallites, and an increase in the surface defects. CeFeO₃ obtained in this study allows for achieving higher CO₂ conversion compared to LaFeO₃ at 600 °C.

Keywords: perovskite; cerium orthoferrite; CeFeO₃; solution combustion synthesis; hydrogenation; CO₂; glycine; urea; urotropine



Citation: Matveyeva, A.N.; Omarov, S.O.; Gavrilova, M.A.; Sladkovskiy, D.A.; Murzin, D.Y. CeFeO₃–CeO₂–Fe₂O₃ Systems: Synthesis by Solution Combustion Method and Catalytic Performance in CO₂ Hydrogenation. *Materials* **2022**, *15*, 7970. <https://doi.org/10.3390/ma15227970>

Academic Editor: It-Meng (Jim) Low

Received: 21 October 2022

Accepted: 9 November 2022

Published: 11 November 2022

Publisher's Note: MDPI stays neutral with regard to jurisdictional claims in published maps and institutional affiliations.



Copyright: © 2022 by the authors. Licensee MDPI, Basel, Switzerland. This article is an open access article distributed under the terms and conditions of the Creative Commons Attribution (CC BY) license (<https://creativecommons.org/licenses/by/4.0/>).

1. Introduction

The limited reserves of fossil crude oil, as well as global warming, and possible consequences for human and environmental safety, are the driving forces for the development of more environmentally friendly and sustainable processes [1]. Among the technological challenges requiring aspectual attention at present are the valorization of biomass, water splitting, CO₂ reduction, abatement of exhaust gases, and production of renewable hydrogen [2,3], which has the potential to replace conventional fossil fuels as a clean energy carrier.

The key to solving and overcoming these challenges is catalysis in combination with solid-state chemistry, which is also used to develop tailor-made catalytic materials, and materials science to elucidate the structure-property relationships in defect solids [4]. Subsequently, many materials that have properties important for successful applications in electronics and other fields, such as crystallinity, particle size, porosity, structure defectiveness, and composition variability, can also be effective catalysts.

In particular, perovskites with their unique physical properties are among such materials that are attracting attention for many materials science applications [5], including

rechargeable batteries [6], supercapacitors [7], photovoltaics [8], photocatalysts [9], and electrocatalysts [10]. Due to the wide range of ions and valences that this structure can contain, as well as the ability to fine-tune perovskites for specific catalytic requirements, these oxides can be successfully applied as catalytic materials [4].

The term perovskite is used to refer to any compound that has a formula ABX_3 and for which the B ion is surrounded by an octahedron of X ions, while the original mineral (perovskite) has the chemical formula $CaTiO_3$ [5].

Oxides with the perovskite structure have a cubic unit cell, where the A ion is at the center of the unit cell, the B ions are located at the corners, and the negative ions occupy the face-centered positions [5,11]. Therefore, “A” ions are large cations and usually belong to the group of alkali or rare earth metals that fit into the dodecahedral sites of the framework and provide structural stability, whereas “B” ions are smaller cations, typically 3d, 4d, or 5d transition metals, occupying octahedral positions of the framework and undergoing redox transformations [12,13]. Generally, in the perovskite framework, the B-site is the catalytically active site, while the A-site plays a major support role [12].

However, most perovskites are deformed due to steric constraints caused by differences in the ionic radii leading to the formation of oxygen/cationic vacancies and changing angles between cations and oxygen. The stability of perovskites relative to other structures is frequently defined in terms of the Goldschmidt tolerance factor (t), the value of which depends on the radii of the cations included in the structure [14,15]. A more detailed description of the structure of perovskites, their various deformations, as well as a definition of their stability, is given in [16–20].

One of the important groups of the perovskite family is rare-earth ferrites, which have recently attracted an increased interest due to the multifunctional properties of many representatives of this class, and the catalysts based on them, are currently used mainly in reduction-oxidation processes [12,13]. $LaFeO_3$, among other ferrites, is the most investigated perovskite, which, due to the partially reduced state of near-surface Fe ions (Fe^{2+}/Fe^{3+}), selectively activates the C-H bond in methane to produce high-purity syngas [13]. For La ferrite, three different types of active iron sites were found, from the point of view of their different surroundings by surface oxygen ions and oxygen vacancies, which determine the completeness of CH_4 oxidation. Unlike lanthanum, cerium ions are characterized by two charge states (Ce^{3+}/Ce^{4+}), which, in combination with Fe^{3+}/Fe^{2+} , suggests that the catalyst based on $CeFeO_3$ can be more active in redox processes than $LaFeO_3$.

Cerium ferrite is still one of the least investigated representatives of this class, although it has the highest abundance in nature among the lanthanide elements [21]. For $CeFeO_3$, an orthorhombic structure of $GdFeO_3$ type is usually expected, because t is 0.85 [20]. Cerium oxide in this perovskite has a possibility of reversible transformation between Ce^{3+} and Ce^{4+} [22]. Increasing the fraction of Ce^{4+} leads to a decrease in oxygen vacancies and in the oxidation state of Fe due to charge neutrality in $CeFeO_3$. The presence of Ce^{4+} and Fe^{2+} slightly distorts the FeO_6 octahedra and increases the tolerance factor to ca. 0.87.

Very few publications addressed the synthesis of $CeFeO_3$, which was structurally described for the first time in [23] because the preparation of $CeFeO_3$ is not as simple as that of other rare earth orthoferrites [24]. Initially, Ce orthoferrites were obtained by firing pressed tablets from a mixture of Fe_2O_3 , CeO_2 , and metallic Fe (as a reducing agent) in a sealed evacuated quartz tube at 800–850 °C for 48 h [25], and under a controlled low partial pressure of O_2 [26]. This method requires a long reaction time, high temperatures, and a complex experimental setup. However, due to the small ionic radius of the Ce^{3+} cation [21], therefore, $CeFeO_3$ is poorly stable in the presence of oxygen and at elevated temperatures. Furthermore, cerium (III) compounds generally tend to oxidize easily to Ce(IV) species, mostly forming stable CeO_2 .

Other synthesis methods have also been proposed, including the co-precipitation method [22,27–29] and sol-gel technique [30,31], which are also complex and/or require high calcination temperatures (550–1000 °C) and long reaction time (3–48 h). At the

same time, there are difficulties in the targeted synthesis of nanostructured CeFeO_3 by these methods.

Thus, taking into account the conceptual difficulties to obtain CeFeO_3 , a feasible alternative is highly desirable. The solution combustion synthesis (SCS) method was explored in this study, as it exhibits such advantages as the short reaction time and the concomitant formation of an inert gas, which prevents oxidation of Ce (III). Overall, SCS is one of the simplest, fast, and most efficient methods for the synthesis of both simple and complex metal oxides [32,33] allowing the production of high-purity homogeneous powders [34].

SCS was proposed by Kingsley and Patil [35] as an alternative to self-propagating high-temperature synthesis (SHS) developed in 1967 by Merzhanov, Shkiro, and Borovinskaya [36]. Before the combustion process, the reactants (salts of metal and organic fuel) are brought into solution, ensuring their uniform distribution. The redox mixture, after evaporation of the solvent, ignites and eventually burns out in a self-sustaining and fast combustion reaction [37].

The fundamental possibility of obtaining CeFeO_3 nanocrystals by SCS was shown in [21,24,37], where glycine or PVA/urea was used as fuel. However, only in some studies was it possible to obtain CeFeO_3 without a noticeable amount of impurity phases. Quantitative phase analysis performed in [24] revealed that the product obtained using glycine-nitrate combustion (fuel-to-oxidizer ratio (φ) of 1.5) consisted of CeFeO_3 with a minor amount of CeO_2 (6.8 wt%). In [21], the optimal fuel-to-oxidizer ratio at which CeFeO_3 is formed with the minimum amount of Fe_2O_3 (ca. 14 wt%) and CeO_2 (ca. 30 wt%) was also found to be 1.5.

In this work, the possibility of CO_2 hydrogenation using CeFeO_3 -containing catalysts prepared by SCS was investigated. CO_2 hydrogenation to CO via the reverse water–gas shift reaction (RWGS, $\text{CO}_2 + \text{H}_2 \rightarrow \text{CO} + \text{H}_2\text{O}$) is one of the most promising processes of CO_2 utilization because CO can be used in the downstream Fischer–Tropsch synthesis (FTS) and other applications [38–41]. The RWGS reaction is also of interest in the context of human missions to Mars, primarily because of its ability to produce water, which is a source of oxygen [42].

The effect of process conditions (fuel, fuel-to-oxidizer ratio, additives) on the physicochemical and catalytic properties of the synthesized materials was also investigated. To highlight the importance and potential of the synthesis method for perovskite-based catalysts, the catalytic efficiency was compared with the literature data.

2. Materials and Methods

2.1. Reagents

$\text{Ce}(\text{NO}_3)_3 \cdot 6\text{H}_2\text{O}$ (99.8%, Chemcraft, Kaliningrad, Russia), $\text{Fe}(\text{NO}_3)_3 \cdot 9\text{H}_2\text{O}$ (98.3%, Lenreactiv, St. Petersburg, Russia), NH_4NO_3 (98.5%, Russia), glycine ($\text{C}_2\text{H}_5\text{NO}_2$, 99.2%, Lenreactiv, St. Petersburg, Russia), glucose ($\text{C}_6\text{H}_{12}\text{O}_6$, 99.8%, Lenreactiv, St. Petersburg, Russia), urea ($(\text{NH}_2)_2\text{CO}$, 99.8%, Lenreactiv, St. Petersburg, Russia), and urotropine ($(\text{CH}_2)_6\text{N}_4$, 99.5%, Russia) were used.

2.2. Synthetic Procedures

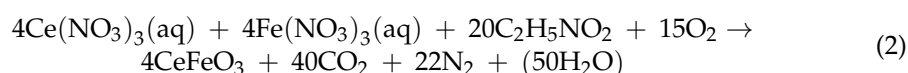
For the preparation of cerium orthoferrite CeFeO_3 , an appropriate amount of the fuel (glycine, glycine-glucose, urea, or urotropine) and the corresponding nitrates were dissolved in deionized water (1 mL of water per 1 g of the starting materials) in a 250 mL wide glass beaker. The weight of the reagents was taken to ensure the synthesis of 1 g of CeFeO_3 . Ammonium nitrate was used in the amounts of 1 g per 1 g of perovskite, while the molar ratio of glucose to glycine was 1:6. The fuel-to-oxidizer ratio (φ) was taken from 1 to 3.7 and calculated according to the following equation [34]:

$$\varphi = (-1)\Sigma(\text{coeff.}\cdot\text{RV of fuel})/\Sigma(\text{coeff.}\cdot\text{OV of nitrate}), \quad (1)$$

where RV—the reducing valency, OV—the oxidizing valency.

In this method, metals, “C” and “H” are considered reducing elements with their corresponding valence, +4 for carbon and +1 for hydrogen. Oxygen and nitrogen are considered oxidizing agents with the valences −2 and 0, respectively [43].

For example, the reaction equation occurring in the process can be represented as:



According to this equation, the reducing valence of glycine ($\text{C}_2\text{H}_5\text{NO}_2$) is +9 ($\text{RV} = 4 \cdot 2 + 1 \cdot 5 + 0 - 2 \cdot 2$), whereas the oxidizing valence of both $\text{Ce}(\text{NO}_3)_3$ and $\text{Fe}(\text{NO}_3)_3$ is equal to −15 ($\text{OV} = 3 - 0 - 2 \cdot 3 \cdot 3$), therefore φ is 1.5 ($-1 \cdot 9 \cdot 20 / (-15 \cdot 4 + (-15) \cdot 4)$).

The obtained solution was heated to boiling on an electric plate (1 kW) and, after complete evaporation of water, was burned with the formation of a solid. Two-three batches of each material were made. Reaction equations for each synthesis are presented in the Supplementary Material.

2.3. Characterization

XRD analysis was done using a SmartLab 3 Diffractometer (Rigaku, Japan) equipped with Ni-filter (Rigaku, Japan) and 1D detector (DteX250, Rigaku, Japan) at the following conditions: $\text{CuK}\alpha$ radiation ($\lambda = 1.54056 \text{ \AA}$), 40 kV, 30 mA, a scan speed of $4^\circ/\text{min}$, and a step width of 0.01° . To determine the phase composition and the crystal structural parameters, the diffraction data were analyzed by the Rietveld method. PDWin software (v. 2.0, 2004) was used for the refinement. The structural parameters for CeFeO_3 with the space group Pbnm, CeO_2 with the space group $\text{Fm}\bar{3}\text{m}$, and Fe_2O_3 with the space group $\text{Fd}\bar{3}\text{mZ}$ were taken using the ICDD PDF-2-2016 database (No. 93611, 193169, and 247036, respectively). The Pseudo-Voigt function was used for the simulation of the peak shape. The background was modeled by a Chebyshev polynomial. The mean crystallite size was calculated using the Scherrer equation.

An infrared transmission spectrum was determined using a IRTracer-100 spectrophotometer (Shimadzu, Japan). The IR spectra were recorded from 4000 to 350 cm^{-1} . One-two mg of each solid sample was mixed with ca. 200 mg of vacuum-dried IR-grade KBr. The mixture was dispersed by grinding in an agate mortar, placed in a steel die 13 mm in diameter, and gradually subjected to a pressure of 12 tons under vacuum pumping.

N_2 -physisorption analysis was performed on ASAP 2020 (Micromeritics, Norcross, GA, USA) and Autosorb-6iSA (Quantachrome Instruments, Boynton Beach, FL, USA). Prior to the measurements, the samples were degassed at 200°C under vacuum. The specific surface area and the total pore volume were determined from N_2 adsorption isotherms applying the BET equation. The pore size distribution was calculated by the DFT (Density Functional Theory) method.

SEM was performed in SE mode using a VEGA 3 SBH microscope (TESCAN, Czech Republic) equipped with Oxford instruments INCAx-act for energy-dispersed X-ray spectroscopy (EDS).

H_2 -TPR was performed on Chemosorb (SOLO, Novosibirsk, Russia) with a thermal conductivity detector (TCD). Before H_2 -TPR, an SCS-product (ca. 60 mg) was pretreated in air to ca. $330\text{--}350^\circ\text{C}$. The reduction was performed from $50\text{--}100$ to 900°C at a ramp rate of $10^\circ/\text{min}$ under 10 vol. % H_2 in Ar (99.998 vol. % purity) and a total gas flow of 20 mL/min. Isopropanol cooled in liquid nitrogen was used as a water trap. CuO was used to calibrate hydrogen consumption.

TGA and DTA were done on a simultaneous thermal analyzer DTG-60A (Shimadzu) by heating a sample in air or nitrogen to 800 °C with a rate of 10 °C/min. The weight measurement error was 1% for TGA and 1 µV for DTA.

2.4. Catalytic Tests

The experiments were carried out in a fixed-bed reactor at atmospheric pressure. Approximately 300 mg of the powder sample (the fraction below 100 µm) was placed on a diffuser grid made of SiO₂ in the cylindrical quartz reactor (37 mm in length, 1.5 cm in inner diameter), which contained a thermocouple pocket with a diameter of 5 mm. The gases were fed into the reactor from top to bottom. The sample was initially heated in the air flow (30 mL/min) to 300 °C, then flushed with N₂ (99.999 vol. % purity, 20 mL/min) up to 400 °C. Thereafter, 50 vol. % H₂ in N₂ was fed with a total flow of 40 mL/min for 1 h. After reduction, the sample was exposed to the reactants at a weight hourly space velocity (WHSV) of 10,000 mL·g⁻¹·h⁻¹ (30 mL/min H₂, 10 mL/min CO₂, and 10 mL/min N₂) for 15 min consecutively at 300, 400, 500, and 600 °C. Nitrogen in the gas flow was used as the internal standard for gas chromatography, allowing the establishment of mass balance. In order to prevent water from entering the GC, the outlet pipe passed through a cooling trap.

For comparison, long-term tests were performed at an elevated WHSV (72,000 mL·g⁻¹·h⁻¹), and a stoichiometric H₂/CO₂ ratio was chosen to evaluate the CO₂ utilization efficiency. After reduction, the sample was exposed to RWGS feed (40 mL/min H₂, 40 mL/min CO₂, and 40 mL/min N₂) at 600 °C for 4 h.

The gas products were analyzed on a GC-2010 Plus chromatograph (Shimadzu) with a TCD (RT-MSieve 5A capillary column (30 m, diameter = 0.53 mm) and Rt-Q-BOND capillary column (30 m, diameter = 0.53 mm); temperature program: 30 °C–5 min; 30–60 °C with a heating rate 4°/min; 60–100 °C with a heating rate 15°/min; 100–150 °C with a heating rate 30°/min; 150 °C–3 min; 150–180 °C with a heating rate 5°/min; 180 °C–23.9 min).

Catalytic behavior was evaluated in terms of CO₂ conversion (*X*, %), selectivity to CO and methane (*S*_{CH₄}, mol%). The following equations were used for calculating:

$$X_{\text{CO}_2} = \frac{\text{Molar flow C from products}}{\text{Molar flow C from CO}_2 + \text{products}} \cdot 100\% \quad (3)$$

$$S_i = \frac{\text{Molar flow C from } i}{\text{Total molar flow C from products}} \cdot 100\% \quad (4)$$

where *i*–CO, CH₄, C₂H₄, C₂H₆, C₃H₈; molar flow C from *i*–molar flow of the product multiplied by the number of carbon atoms in the compound, mol/h; total molar flow C = *n*(CO) + *n*(CH₄) + 2·*n*(C₂H₄) + 2·*n*(C₂H₆) + 3·*n*(C₃H₈), mol/h.

The deactivation rate (*k_d*) with time-on-stream (*t*) was calculated with the assumption that the deactivation follows first-order kinetics as follows:

$$k_d = \frac{1}{t} \left(\ln \frac{1 - (X_{\text{CO}_2})_t}{(X_{\text{CO}_2})_t} - \ln \frac{1 - (X_{\text{CO}_2})_0}{(X_{\text{CO}_2})_0} \right) \quad (5)$$

where (*X*_{CO₂})₀ is the initial conversion of CO₂; (*X*_{CO₂})_{*t*}–the conversion of CO₂ at time *t*.

The rate of CO₂ hydrogenation (*r*, mmol·s⁻¹·g⁻¹) was calculated using the following equation:

$$r = \frac{X_{\text{CO}_2} \cdot F_{\text{CO}_2}}{m_{\text{cat}}} \quad (6)$$

where *F*–the CO₂ flow rate (mmol/s), *m_{cat}* is the catalyst weight (g).

3. Results and Discussion

3.1. Synthesis Features and Phase Composition

Based on the previous studies on the synthesis of CeFeO₃ with the solution combustion method [21,24], the first syntheses were carried out using glycine as fuel with a fuel-to-

oxidizer ratio of 1–1.5. Figure 1 shows the visual course of the combustion and the macro morphology of the obtained SCS products.

It can be clearly seen from Figure 1 that combustion in the specified range of φ proceeds quite efficiently in a self-propagating mode. Abundant gas evolution leads to the formation of the fluffy powders. Despite incremental changes in the fuel-to-oxidizer ratio, the morphology and the color of the obtained solid products have changed significantly. Qualitatively, it is possible to predict the presence of the Fe_3O_4 (magnetite) phase in the samples in small amounts, judging by the dominance of the deep black color. The DTA curves (Figure 2), respectively, also indicate the presence of magnetite, which at ca. 300 °C turns into $\gamma\text{-Fe}_2\text{O}_3$, and the latter at ca. 600 °C undergoes a transformation into $\alpha\text{-Fe}_2\text{O}_3$ (hematite) [44]. An increase in the mass of the samples upon heating in air in the range from 300 to 800 °C (Figure 2) indicates the presence of cerium orthoferrite, which undergoes oxidation according to the following reaction [45]: $6\text{CeFeO}_3 + \text{O}_2 = 6\text{CeO}_2 + 2\text{Fe}_3\text{O}_4$. The largest weight gain occurs when heating the sample obtained at a fuel (glycine)-to-oxidizer ratio of 1.4.



Figure 1. The course of the fuel-nitrate solution combustion and the macro morphology of the SCS products obtained at various fuel-to-oxidizer ratios.

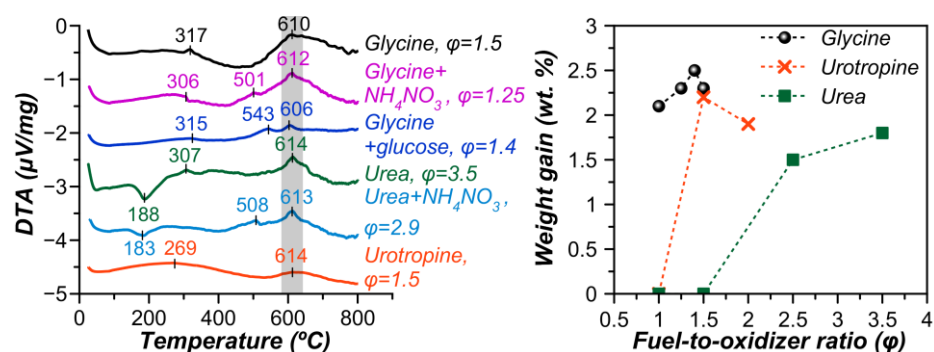


Figure 2. Differential thermal curves and weight gain during heating in air for the as-prepared samples produced by SCS using different fuels, additives, and fuel-to-oxidizer ratios.

XRD measurements prove the successful synthesis of the rare earth orthoferrite CeFeO_3 by glycine-nitrate solution combustion synthesis (Figure 3a). However, in all cases, there are side phases of $\gamma\text{-Fe}_2\text{O}_3/\text{Fe}_3\text{O}_4$, which are difficult to distinguish by XRD analysis, and

cubic CeO_2 . It is believed that oxidation of a small amount of Ce(III) to Ce(IV) can occur before the ignition of the solution [24].

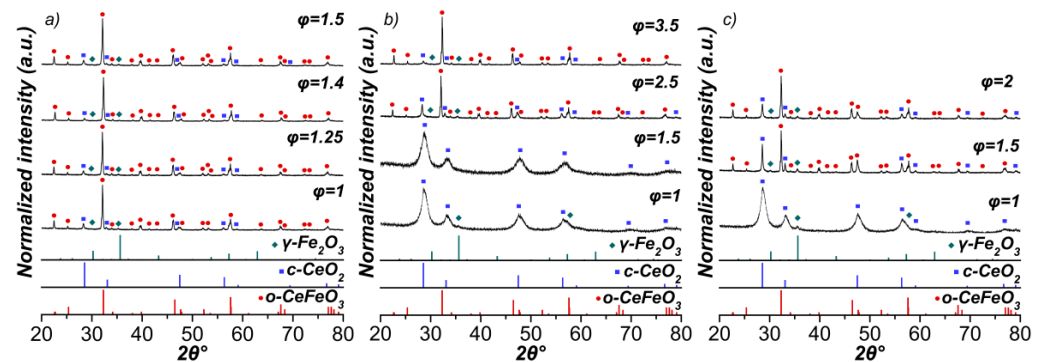


Figure 3. XRD patterns of synthesized materials by (a) glycine-nitrate; (b) urea-nitrate; and (c) urotropine-nitrate combustion at the various fuel-to-oxidizer ratios (φ) (where o- CeFeO_3 —orthorhombic perovskite CeFeO_3 (JCPDS card no. 00-022-0166); c- CeO_2 —cubic CeO_2 (JCPDS card no. 01-075-8371); γ - Fe_2O_3 —cubic Fe_2O_3 (JCPDS card no. 00-039-1346)).

Compared to glycine, combustion in the presence of urea proceeds with an intensive flame both at a stoichiometric fuel-to-oxidizer ratio and upon an excess of urea $\varphi = 2.5$ (Figure 1). The extra heat from the urea combustion promoted sintering through enhanced diffusion. However, only at $\varphi = 2.5$ and more, was it possible to obtain the Ce orthoferrite phase (Figure 3b). According to the total weight change (Figure S1), despite the formation of orthoferrite, a very large amount of unburned fuel remained at $\varphi = 3.5$. This was also confirmed by IR spectroscopy showing intense bands of functional groups corresponding to the fuel (Figure 4, Table S1).

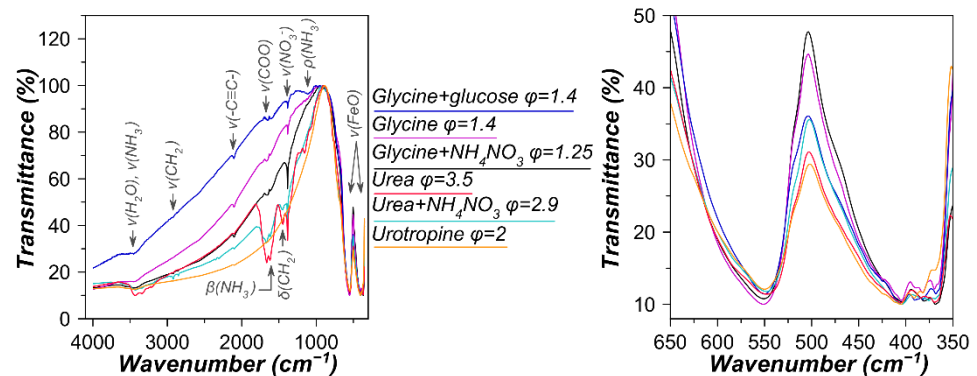


Figure 4. IR spectra of the as-prepared samples produced by solution combustion synthesis using different fuels, additives, and fuel-to-oxidizer ratios (φ).

Unlike glycine and urea, urotropine (hexamethylenetetramine) with lower enthalpy of combustion [46,47] has not been previously used to obtain cerium orthoferrite. No obvious ignition was noticed and combustion proceeded in a smoldering mode (Figure 1). In the case of a stoichiometric ratio, a glass beaker could not resist a large heat release. Nevertheless, at $\varphi = 1.5$ and 2, it was possible to synthesize CeFeO_3 perovskite, despite a higher content of impurity phases compared with the use of other fuels (Figure 3c), Table 1).

For the SCS products containing reflections of cerium orthoferrite, structural studies were carried out with refinement by the Rietveld method. The quantitative phase composition and the average crystallite size (D) are presented in Table 1. For some samples, the Rietveld method was not applicable to calculate the content of Fe_2O_3 . This suggests that the Fe_2O_3 particles are very small and highly dispersed on the surface or the content of free Fe_2O_3 is below the detection limit of XRD. Similar data were obtained in [24], where

iron oxide was also not taken into account in the composition. The phase composition was corrected considering amorphous iron oxide based on the CeO₂ content obtained by the Rietveld method. Table S2 contains data to benchmark the reproducibility of the synthesis results from batch to batch. The composition and the size of the orthoferrite crystallites have good reproducibility (4.5 and 6.5%, respectively), while the crystallite size of oxide phases was less efficiently reproduced due to low content of these phases.

Table 1. Data on the phase composition and crystallinity of the synthesized materials according to the refinement by the Rietveld method.

Sample N	Fuel	n(AN)/n(MeN)	φ	Phase Composition According Rietveld/Corrected ¹ , wt%			D (1), nm	D (2), nm	D (3), nm	R _{wp} /R _e
				CeFeO ₃	CeO ₂	Fe ₂ O ₃				
1	Glycine	–	1	81/74	19/18	0/8	67.5	4.7	–	–
2	Glycine	–	1.25	78	12	10	66.0	7.5	6.7	1.14
3	Glycine	–	1.4	95/93	5/5	0/2	61.3	25.0	–	1.16
4	Glycine	–	1.5	87/82	13/12	0/6	56.8	9.0	–	–
5	Glycine	1.5	1.25	96/94	4/4	0/2	69.1	15.6	–	1.13
6	Glycine	1.5	1.75	33	47	20	32.7	14.8	14.7	1.03
7	Glycine + glucose	–	1.4	63	23	14	52.0	19.4	14.3	–
8	Urea	–	2.5	52	28	20	68.6	5.8	4.0	–
9	Urea	–	3.5	80	13	7	72.0	4.7	6.3	1.09
10	Urea	1.5	2.9	91/87	9/7	0/4	66.5	22.0	–	1.17
11	Urotropine	–	1.5	48	33	19	75.1	22.1	15.8	–
12	Urotropine	–	2	61	23	16	60.0	16.4	7.1	1.09

¹ Taking into account amorphous iron oxide according to the equation $\text{wt}\%(\text{Fe}_2\text{O}_3) = \text{wt}\%(\text{CeO}_2)/2.156$, where 2.156 is CeO₂/Fe₂O₃ ratio obtained at oxidation of CeFeO₃; AN—ammonium nitrate; MeN—cerium and iron nitrates; φ—the fuel-to-oxidizer ratio; D—the mean crystallite size; 1—CeFeO₃; 2—CeO₂; 3—γ-Fe₂O₃; R_{wp}/R_e characterizes goodness of fit, if the squared value is equal to one or constant the refinement procedure is complete.

The largest amount of CeFeO₃ (ca. 93 wt%) was obtained using glycine as a fuel at φ = 1.4, while urotropine, on the contrary, led to the lowest content of the target phase. The average size of CeFeO₃ crystallites ranges from ca. 49 to 75 nm depending on the fuel and its amount, which directly affects the combustion temperature. A higher temperature of combustion during SCS generally results in a larger particle size, stronger agglomeration, and a lower specific surface area of the products. At the same time, higher amounts of released gases increase porosity and the specific surface area. Therefore, the pore structure is a compromise of the combustion temperature, as well as the type and amount of the gaseous products [48,49]. For example, with the same ratio of the fuel-to-oxidizer equal to 1.5, glycine, due to the lower combustion temperature and high gas evolution, afforded more dispersed particles of orthoferrite compared to urotropine (Table 1).

The influence of ammonium nitrate and glucose addition to the fuel on the purity of cerium orthoferrite was also studied (Table S3). Neat ammonium nitrate as a strong oxidizing agent supports and accelerates fuel combustion. It was observed that upon adding 1 g NH₄NO₃ to a mixture of glycine with metal nitrates, the amount of formed perovskite increased from ca. 82 (N.4, Table 1) to ca. 94 wt% (N.5). A similar situation occurs during firing with urea when the yield of perovskite increased from 80 to 87 (N.9 and 10, Table 1). This phenomenon can apparently be explained by an increase in the formation of gases that prevent the oxidation of orthoferrite. Such Ce orthoferrite content is the highest obtained by the SCS method among previously published studies (96 versus 93 wt% [24], excluding iron oxide).

Glucose, as a typical carbohydrate, being a large and bulky molecule, tends to leave large voids while burning. Combustion of glycine with glucose is accompanied by the ejection of the sample in the form of fragile filaments (see Table S3). Despite this, the Ce orthoferrite content is greatly reduced from 74 to 63 wt% (N.1 and 7, Table 1).

The size of crystallites in Ce-Fe oxide systems was also analyzed. Reflections of iron oxide are poorly detected (Figure S2), therefore the results in Table 2 are presented for

only CeO_2 . The smallest size of ceria was obtained by using glycine and glucose at a high fuel-to-oxidizer ratio, but in this case, almost a third of the fuel was not burned (N.13, Table 2). Urea and urotropine at $\varphi = 1$ have led to approximately the same size of crystallites and weight losses.

Table 2. The mean size of CeO_2 crystallites (D) and total weight loss for Ce-Fe oxide systems obtained by the SCS method using various types of fuel and the fuel-to-oxidizer ratio.

Sample N.	Fuel	φ	D (CeO_2), nm	Total Weight Loss According to DTA, wt%
13	Glycine + glucose	2.2	1.9	29.6
14	Urea	1	5.7	4.6
15	Urea	1.5	5.0	4.4
16	Urotropine	1	6.5	5.5
17	Urotropine	6	4.7	–

3.2. Structural and Textural Properties

SEM images of the powders prepared using different types of fuel are shown in Figure 5. For all SCS products, micrographs reveal a porous foam-like network of agglomerated interconnected particles. As can be seen, when using glycine (Figure 5a–c), in contrast to urea (Figure 5d,e) and urotropine (Figure 5f), it is not possible to reveal pronounced grain boundaries in the samples, crystals of which have coalesced into each other. This can be attributed to a lower flame temperature reached for the reaction between glycine and nitrates [47].

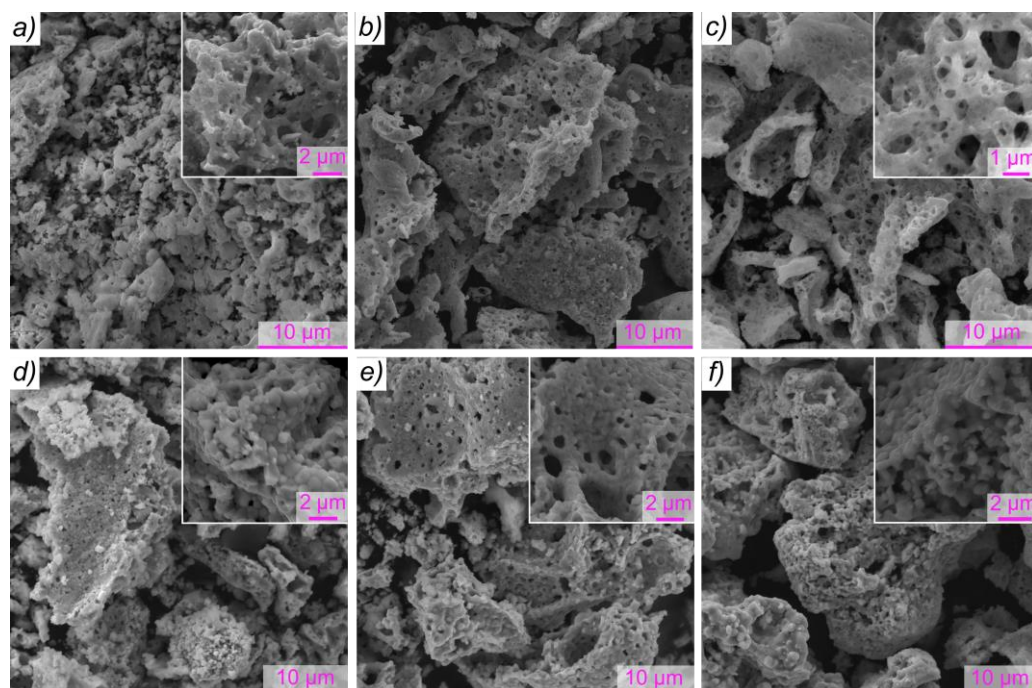


Figure 5. SEM images of the SCS products obtained using different fuels and additives (the upper-right inset shows the corresponding high magnification image): (a) glycine, $\varphi = 1.4$; (b) glycine and NH_4NO_3 , $\varphi = 1.25$; (c) glycine and glucose, $\varphi = 1.4$; (d) urea, $\varphi = 3.5$; (e) urea and NH_4NO_3 , $\varphi = 2.9$; (f) urotropine, $\varphi = 2$.

Fuel type, as well as the fuel-to-oxidizer ratio, can strongly affect closed and open porosity, the average thickness of the pore wall, etc. The most porous sample, as expected, was prepared using glucose as an additive to glycine (Figure 5c). In turn, the dimensional restrictions of the pore walls (a neck) can affect the phase composition of the SCS products. Insufficient pore wall thickness for the formation of an orthoferrite phase stable under the given conditions can be the reason for the formation of more stable products (CeO_2 ,

Fe₂O₃) with smaller crystallites [21]. This explains a decrease in the content and diameter of cerium orthoferrite crystallites upon using glucose (Table 1).

To estimate the specific surface area (S_{BET}) and the total pore volume (ΣV_{pore}), low-temperature N₂ adsorption-desorption was performed, the results of which are presented in Table 3 and Figure 6. S_{BET} for samples with a high content of CeFeO₃ (80–94 wt%) turned out to be extremely low (2–3 m²/g). A sample prepared using glucose as a second fuel allowed a slight increase in the specific surface area to ca. 8 m²/g compared to a sample with the same CeFeO₃ content obtained by urotropine-nitrates combustion (N.12, Table 3). No positive effect of NH₄NO₃ on the porosity characteristics of the obtained materials has been found in this study, in contrast to [50], where the use of ammonium nitrate with a mixture of urea and metal nitrates increased the specific surface area of perovskite LaMnO₃ from 4 to ca. 20 m²/g. The sample containing only iron and cerium oxides has a fairly large specific surface area of ca. 81 m²/g (N.15, Table 3), which is in fact larger than that of the Ce–Fe oxide system obtained by coprecipitation (14 m²/g, [51]).

Table 3. Textural characteristics of the as-prepared samples produced by solution combustion synthesis using different fuels, additives, and fuel-to-oxidizer ratios (φ).

Sample N.	Fuel, Additive, φ	Mass Fraction of CeFeO ₃	S_{BET} , m ² /g	ΣV_{pore} , cm ³ /g	Average Pore Size, nm
3	Glycine, 1.4	0.93	3	0.01	16.5
5	Glycine, NH ₄ NO ₃ , 1.25	0.94	2	0.01	15.0
7	Glycine, glucose, 1.4	0.63	8	0.12	60.5
9	Urea, 3.5	0.80	3	0.05	59.0
12	Urotropine, 2	0.61	4	0.05	47.5
15	Urea, 1.5	0	81	0.13	6.3

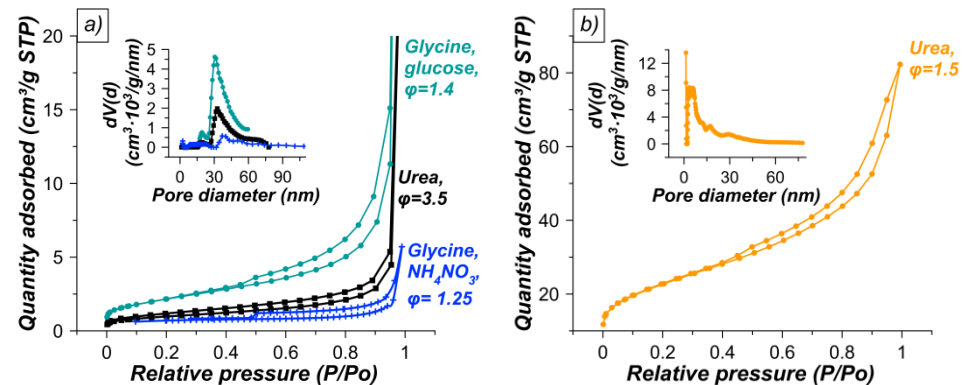


Figure 6. N₂ adsorption-desorption isotherms and pore size distribution for (a) the as-prepared CeFeO₃–CeO₂–Fe₂O₃ and (b) CeO₂–Fe₂O₃ systems produced by SCS using different fuels, additives, and fuel-to-oxidizer ratios (φ).

All SCS products have an IUPAC type IV(a) isotherm [52], which is typical of a mesoporous structure. Apparently, small volumes of mesopores are formed due aggregation of small crystalline particles. The hysteresis loop is of the H4 type, often found in aggregated crystals. The pore size distribution for the perovskite-containing system (Figure 6a) is relatively wide, with maxima of ca. 20 and 30–40 nm compared to the Ce–Fe oxide system, which has a narrower pore size distribution with a maximum of ca. 4 nm (Figure 6b).

3.3. Reducibility

Because reducibility is an important factor influencing the catalytic efficiency of a perovskite, an H₂-TPR analysis was performed. The reduction process leads to complex TPR profiles and depends on the phase composition, as can be seen in Figure 7. The corresponding amounts of hydrogen consumed in the various reduction steps, as well as

the corresponding calculated amounts of hydrogen required for the reduction of Fe_2O_3 and CeO_2 , are summarized in Table 4.

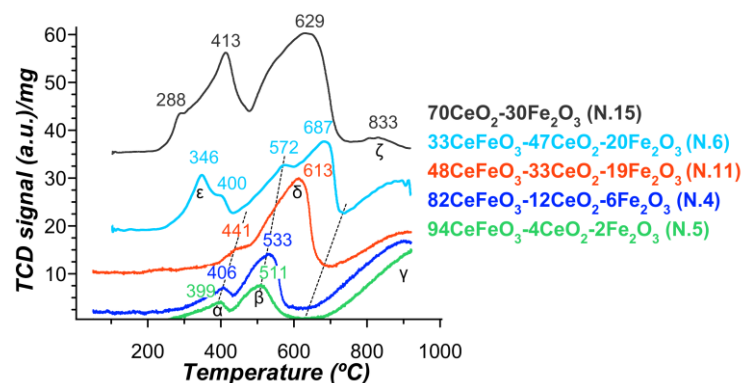


Figure 7. Temperature-programmed reduction (TPR) spectra of the SCS-products calcined at 330–350 °C.

Table 4. H_2 -TPR results and cell parameters for studied in TPR samples.

Sample	Unit-Cell Volume (CeFeO_3), \AA^3	Lattice Parameter (CeO_2), \AA	Theoretical H_2 Uptake ¹ , mmol/g			H_2 Uptake According to TPR, mmol/g			
			CeO_2	Fe_2O_3	Total	Area 1 ($\alpha + \epsilon$)	Area 2 ($\beta + \delta$)	Area 3 ($\gamma + \zeta$)	Total
N.15	–	5.376	2.05	6.15	8.20	3.77	5.42	0.7	9.89
N.6	240.120	5.406	1.37	3.76	5.12	1.37	4.49	1.98	7.84
N.11	239.833	5.408	0.96	3.57	4.53	1.13	2.82	2.82	6.77
N.4	239.511	5.402	0.35	1.13	1.48	0.73	1.29	5.23	7.25
N.5	239.930	5.396	0.12	0.38	0.49	0.62	0.78	5.69	7.09

¹ Assuming a complete reduction up to Ce_2O_3 and Fe^0 , respectively.

For all samples, the presence of free iron oxide was noted, although in different amounts. It is well known that the reduction of Fe_2O_3 proceeds via Fe_3O_4 (magnetite) and FeO (wüstite) to iron [53–55]. The formation of FeO is often not observed since it is metastable and disproportionates into Fe_3O_4 and Fe below 620 °C [56]. According to the authors of [53], in the stepwise reduction of iron oxide, the experimental TPR profile of Fe_2O_3 contained two peaks at 394 and 545 °C, which correspond to Fe_3O_4 and $\text{FeO} + \text{Fe}$, respectively. The ratio of the area of the first peak to the area of the second peak should be close to 1:8.

Three reduction steps were observed on the reduction profiles of samples with a high CeFeO_3 content (48–94 wt%) centered at: 399–441 °C (peak α); 511–613 °C (peak β); and above 650 °C (peak γ), which did not reach the end at 900 °C. The reduction of perovskite CeFeO_3 mainly occurs at temperatures above 650 °C. In the case of a sample containing 94 wt% CeFeO_3 , the amount of hydrogen consumed in the first two steps is almost three times higher than expected. Thus, it cannot be excluded that surface iron ions from perovskite started to be reduced at lower temperatures. In addition, the ratio of the first two peaks is 0.8. This is due either to an increased amount of Fe^{2+} in free FeO_x and the surface of CeFeO_3 , as well as the formation of oxygen-deficient CeO_x , or the formation of cation-deficient CeFeO_3 . The first leads to an increase in the anion defectiveness of the system. In the second case, changing the number of A or B ions will initially lead to an increase in the charge of the corresponding B or A cations, similar to LaFeO_3 with a deficiency of La [57]. However, at the stage of reductive activation, as well as during a catalytic process, their reduction and formation of additional oxygen vacancies are expected.

According to the literature [58], iron is mainly present in the +3-oxidation state in an AFeO_3 perovskite (where A is a rare earth metal), therefore, the following reduction steps can be proposed [59,60]: (1) the partial reduction of Fe^{3+} (clustered and surface) to Fe^{2+} ; (2) complete reduction of Fe^{3+} (aggregated) to Fe^{2+} , with a possible additional consumption

of hydrogen for the surface reduction of Fe^{2+} ; (3) reduction of the remaining Fe^{2+} to Fe^0 and obtaining individual phases of Ce_2O_3 and Fe.

$\text{CeO}_2\text{-Fe}_2\text{O}_3$ and a sample with a low CeFeO_3 content (33 wt%, N.6) exhibit similar, although more complex profiles, as two additional peaks δ and ϵ appear at $\sim 288\text{--}346$ °C and $\sim 629\text{--}687$ °C. These peaks can hardly be attributed to cerium oxide, despite its high content. For pure CeO_2 , two characteristic peaks are usually observed at ca. 500 and 800 °C [61,62], which are associated with the reduction of surface and bulk oxygen, respectively. However, the $\text{CeO}_2\text{-Fe}_2\text{O}_3$ system has only a low-intensity CeO_2 peak at ca. 800 °C (peak ζ), thus the low-temperature peak should also be of low intensity.

In the case of the Ce–Fe oxide system, CeO_2 (002) reflection is also shifted toward larger diffraction angles, and the lattice parameters of cerium decrease to 5.376 Å (Table 4), which indicates the formation of a $\text{Ce}_{1-x}\text{Fe}_x\text{O}_{2-d}$ solid solution after the replacement of Ce^{4+} (0.97 Å) to Fe^{3+} with a smaller size (0.64 Å) inside the structure of the cubic phase of CeO_2 . This leads to the formation of oxygen vacancies owing to the charge balance [56,61]. It was shown in [56] that the reduction ability increases with the close interactions of Fe and Ce cations.

Therefore, Fe_2O_3 in the Ce–Fe oxide system undergoes a three-stage reduction of Fe_2O_3 to Fe_3O_4 (413 °C), Fe_3O_4 to FeO (ca. 550 °C), and then to Fe (629 °C), as can be confirmed by 2D XRD pattern recorded during $\text{H}_2\text{-TPR}$ for 70Ce–Fe [51]. Regarding the peak at $\sim 288\text{--}346$, it can be associated according to [63] with dispersed Fe.

In summary, the results of the characterization revealed that the phase transformation of the synthesized materials is strongly affected by the amount of perovskite. To evaluate the impact on catalytic properties, the samples with different amounts of CeFeO_3 were tested in CO_2 hydrogenation.

3.4. Catalytic Performance

Figure 8 shows the catalytic behavior of the samples as a function of reaction temperature and perovskite content. As expected, the temperature has a critical effect on CO_2 conversion. Elevation of temperature resulted in lower apparent activation energy, which can be associated with a change in the kinetic regime through the regime of internal mass transfer limitations to the regime of limitations by external diffusion (Figure S3). It was found that some samples are more active at temperatures of 300–400 °C, while others are more active at 500–600 °C. The observed activation energy for CO_2 hydrogenation in the range of 300–400 °C was determined to be 101 kJ/mol for the Ce–Fe oxide system (N.14), and 87 kJ/mol for the material containing CeFeO_3 (N.5). These data generally correspond to the literature data, where the activation energy was reported to be 80 kJ/mol for Fe_3O_4 (327–427 °C), and 110 kJ/mol for an industrial catalyst $\text{Cu/ZnO/Al}_2\text{O}_3$ (170–260 °C) [64].

With increasing the perovskite content no clear trends in conversion could be seen; therefore, it is quite probable that iron oxide, and not only perovskite, is also responsible for the activity of all samples. CO_2 hydrogenation over Fe-based catalysts has been extensively investigated because they contain active sites necessary to realize the two catalytic reactions in this process: CO production by reverse water gas shift reaction (RWGS) and Fischer–Tropsch synthesis (FTS) with hydrocarbon formation [65].

The dominant product for all samples, and for many even the only one, is CO. For the three most active samples (N.5, 6, 10) at a low reaction temperature, the formation of $\text{C}_1\text{--C}_3$ hydrocarbons is observed (Figure 8). High RWGS activity and absence of FTS have been found earlier for Fe oxide phases that did not form carbides as a result of carburization under conditions of CO formation [66]. It has been established that FeC_x species are formed by the conversion of surface layers of the Fe_3O_4 phase [67]. In addition, in the presence of a carburizing environment (CO_2/H_2), Fe^0 species could be quickly transformed into hexagonal iron carbides [68,69]. Fe_2O_3 as well as Fe are not active in Fischer–Tropsch synthesis and hydrocarbon formation starts only after partial carburization [66,67,70]. Thus, the increased activity of some samples at low temperatures is indirect evidence of Fe_3O_4 , Fe, and carbide phase formation during the reaction. It is stated in the literature that oxide and

carbide nanoparticles of Fe located in close proximity to each other provide active sites for RWGS and FTS [71–73]. At the same time, CO₂ conversion and selectivity to hydrocarbons depend on the ratio of Fe₃O₄ and Fe₅C₂ phases [74].

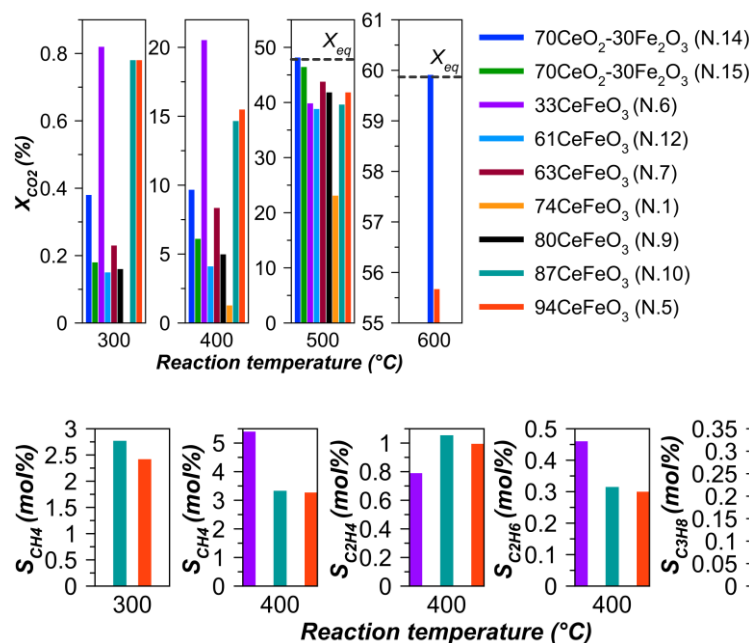


Figure 8. Dependence of CO₂ conversion and selectivity to hydrocarbons on temperature at H₂:CO₂:N₂ = 3:1:1, WHSV = 10 000 mL·g⁻¹·h⁻¹. CO selectivity is 100 mol%, except for samples additionally generating hydrocarbons (N. 5, 6, 10).

XRD did not detect iron carbide in the spent catalysts (Figure 9), which is probably due to its small amount, in line with low selectivity to hydrocarbons. The only new phase is metallic iron, which appeared in the XRD patterns of the samples tested at 500 °C and a high contact time (0.36 s). The Ce–Fe oxide system has the highest metallic iron content after the reaction. In [75], an increase in the amount of surface Fe⁰ species in the freshly reduced catalysts led to a linear decrease in methane yield.

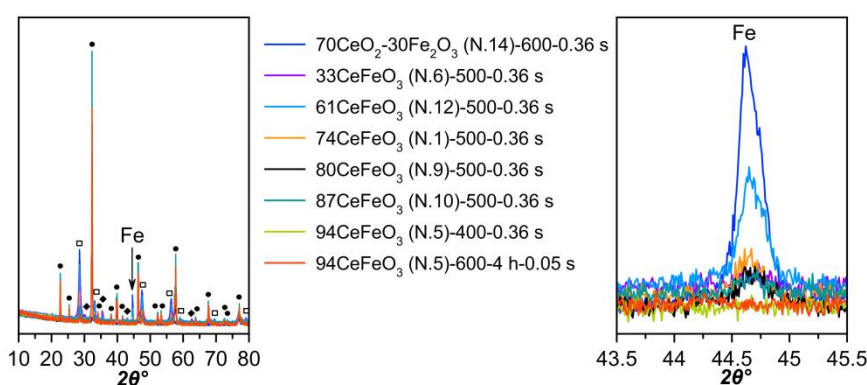


Figure 9. X-ray diffraction patterns of spent catalysts (the legend indicates the tested temperature, residence time, and TOS). ●—o—CeFeO₃ (JCPDS card no. 00-022-0166); □—cubic CeO₂ (JCPDS card no. 01-075-8371); ◆—γ-Fe₂O₃ (JCPDS card no. 00-039-1346).

On the other hand, a contribution to the increase in activity is also possible due to the presence of cerium. Compared to CeO₂ and Fe₂O₃, mixed samples of CeO₂–Fe₂O₃ displayed increased activity, especially 20 wt% CeO₂ [51]. Moreover, a combination of both oxides efficiently suppresses the sintering and improves stability in CO₂ reduction to

CO by chemical looping. The effect of ceria can also be associated with the formation of a Ce–Fe oxide solid solution that increases the specific surface area and, possibly, increases the electron density on Fe atoms in active carbide phases, acting as a main electronegative promoter [76]. Therefore, the catalytic performance depends both on the activity of each active phase and on their spatial distribution, and close contact between them.

The samples that are most active at low temperatures have in common the utilization of ammonium nitrate as an additive to the oxidizer. The flash pyrolysis of NH_4NO_3 is known to yield N_2 , H_2O , and O_2 , excluding a possibility of NO_x formation [77]. An increased gas formation could push the oxide phases to the surface of ferrite and increase their reactivity.

Dependences of CO_2 conversion on time-on-stream and CH_4 selectivity on conversion for the material active in the FTS reaction are presented in Figure 10a. It can be seen that there is a synchronous decrease in conversion and selectivity. The main deactivation factor is usually considered to be coke deposits as a result of secondary reactions [78]. In addition, it is clearly seen from Figure 10a that non-zero selectivity to CH_4 is anticipated at a very close to zero conversion of CO_2 , which implies that CO_2 is directly (without intermediate CO formation) hydrogenated to CH_4 [79].

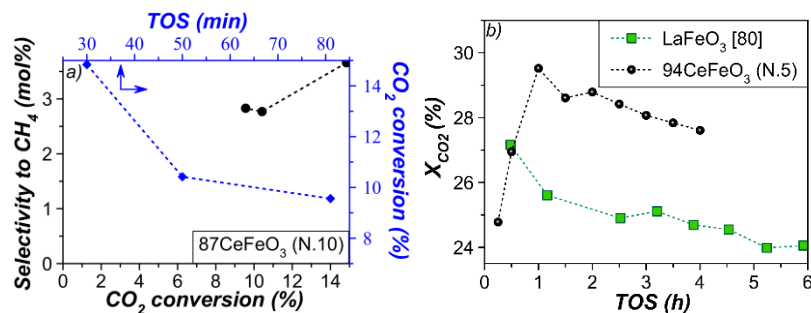


Figure 10. Dependence of CO_2 conversion and selectivity to CH_4 on time-on-stream (TOS) at (a) 400 °C, $\text{H}_2:\text{CO}_2:\text{N}_2 = 3:1:1$, $\text{WHSV} = 10,000 \text{ mL}\cdot\text{g}^{-1}\cdot\text{h}^{-1}$; and (b) 600 °C, $\text{H}_2:\text{CO}_2:\text{N}_2 = 1:1:1$, $\text{WHSV} = 72,000 \text{ mL}\cdot\text{g}^{-1}\cdot\text{h}^{-1}$.

To provide a final comparison of the samples obtained in this study with other perovskite-based catalysts previously applied for CO_2 hydrogenation, their activity was compared under the same reaction conditions. In [80], LaFeO_3 was tested at 600 °C, WHSV of $72,000 \text{ mL}\cdot\text{g}^{-1}\cdot\text{h}^{-1}$, and H_2/CO_2 ratio of 1. The sample containing 94 wt% CeFeO_3 perovskite demonstrated a higher conversion with 100 mol% CO selectivity compared to LaFeO_3 (Figure 10b). In the first hour of the reaction, an induction period of catalyst activation is observed, during which the activity increases from 24.8 to 29.5%, due to the residual reduction of iron oxides. The deactivation rate constant (k_d) was the same as for LaFeO_3 (0.02 h^{-1}). In fact, in this case, deactivation is slower than in the case of a commercial catalyst ($k_d = \sim 0.13 \text{ h}^{-1}$, 5 h of TOS [81]).

It was suggested that the activity of LaFeO_3 is due to the abundance of oxygen vacancies, which contribute to CO_2 activation [80]. For the CeFeO_3 catalyst, the synergy between the phases is explained by the creation of a large amount of oxygen vacancies in the presence of CeFeO_3 and CeO_2 stimulating the migration of oxygen ions, while iron species on the surface promote a pathway of the oxygen spillover from subsurface to surface and improve lattice oxygen transfer [82,83]. CO_2 adsorption and dissociation on CeO_2 surface defects followed by the formation of carbonates and formates are also often considered as the reaction mechanism for the RWGS reaction over CeO_2 -supported catalysts [84,85]. The presence of a large amount of Fe^0 in the $\text{Fe}_2\text{O}_3\text{--CeO}_2$ composite and the oxygen deficiency of CeFeO_3 obtained using NH_4NO_3 can contribute to a change in the reaction mechanism. Both systems are generally characterized by the redox mechanism; however, for defective CeFeO_3 , the role of associative mechanisms seems to also increase at 300–400 °C [85].

CO₂ hydrogenation for the catalyst and some materials reported in the literature are presented in Table 5. The CeFeO₃-based catalyst exhibited a similar or even higher CO₂ hydrogenation rate compared to some other recently reported materials, including the commercial catalyst Cu/ZnO/Al₂O₃.

Table 5. Comparison of catalyst selectivity and CO₂ conversion rate, P = 1 atm, T = 600 °C.

Catalyst	H ₂ :CO ₂	WHSV, mL·g ⁻¹ ·h ⁻¹	CO Selectivity, %	Rate (mmol CO ₂ /(g _{cat} ·s))	Ref.
94CeFeO ₃ -CeO ₂ -Fe ₂ O ₃	1:1	72,000	100	0.064	This work
5Cu/LaFeO ₃	1:1	72,000	100	0.10	[80]
Commercial Cu/ZnO/Al ₂ O ₃	2:1	300,000	100	0.076	[81]
CuAl ₂ O ₄	2:1	300,000	100	0.005	[81]
Cu-Fe/SiO ₂	1:1	120,000	no data	0.037	[86]
5Fe/CeO ₂	1:1	600,000	no data	0.389	[87]

It was also considered how much carbon dioxide emissions are generated during the synthesis of the materials compared to the catalytic process. The mass balance is presented in Table S4. For the calculations, a reaction equation was used giving the maximum formation of perovskite, that is, the one corresponding to glycine and NH₄NO₃ as reagents. Excluding ammonium nitrate, the fuel-to-oxidizer ratio is 1.5, meaning that because of a slight excess of fuel more gases are released.

During the synthesis of 1 g of perovskite, ca. 0.9 L of CO₂ is released. Therefore, there is less carbon dioxide per 300 and 100 mg of the catalyst (shown in Table S5). Based on the conditions of the experiments carried out in this study, the time to reach the conversion corresponding to released amounts of CO₂ during the synthesis of the perovskite was calculated. Such time depends on conversion and WHSV. On the other hand, the catalyst can operate for a long time both with or without regeneration. Therefore, it can be concluded that the amount of reacted carbon dioxide through its hydrogenation exceeds the amount of CO₂ formed during the synthesis of perovskites.

4. Conclusions

In this study, solution combustion synthesis has been successfully applied for the preparation of CeFeO₃ perovskite-based catalysts, which were investigated for the first time in CO₂ hydrogenation. Hydrogenation of CO₂ from industrial exhaust gases via the reverse water–gas shift reaction (RWGS) to CO represents one of the most promising CO₂ utilization processes because CO can be used in the downstream Fischer–Tropsch (FTS) reaction and other applications. The driving force for the development of new systems for this process is the low thermal stability of industrial copper-based catalysts at high temperatures and, therefore, their rapid deactivation because of sintering and reoxidation. CeFeO₃, in turn, is highly stable under reducing conditions and, due to its defective structure, has the potential to be used in CO₂ hydrogenation.

The solution combustion synthesis method represents an alternative to the traditional techniques due to its short synthesis time, low cost, and energy savings, while the main drawback is associated with the formation of pollutant gases, NH₃ or NO_x. In this respect, SCS is similar to other methods when nitrate precursors are used. To achieve the highest yield of cerium orthoferrite, several fuels were used, such as glycine, urea, and urotropine, as well as such additives as glucose and ammonium nitrate. NH₄NO₃ prevents oxidation of Ce(III) to Ce(IV), which is usually an undesirable side reaction. In combination with glycine, NH₄NO₃ makes it possible to obtain the highest yield of cerium orthoferrite (94 wt%). Depending on the synthesis conditions, the combustion products had different phase compositions, crystallinity, specific surface area, and reducibility, the effect of which was evaluated in CO₂ hydrogenation.

Various CeFeO₃-CeO₂-Fe₂O₃ systems containing from 0 to 94 wt% CeFeO₃ have shown that RWGS reaction is dominant in the CO₂ hydrogenation process. At the same time, it was found that samples prepared using ammonium nitrate are more active at temperatures of 300–400 °C and form hydrocarbons (CH₄, C₂H₄, C₂H₆, and C₃H₈) in

addition to CO. The best catalytic performance in CO₂ hydrogenation at low temperatures and the H₂:CO₂ ratio of 3:1 was obtained with a sample containing 33% CeFeO₃ prepared using glycine and ammonium nitrate.

At 600 °C and the H₂:CO₂ ratio of 1:1, the CeFeO₃-based catalyst exhibits higher activity than another member of the rare-earth orthoferrite class LaFeO₃. Activity can be enhanced by the presence of unbound cerium and iron oxides, due to the fact that Ce–Fe perovskite and CeO₂ phases can produce more oxygen vacancies and promote migration of the oxygen ion, while surface iron particles facilitate the oxygen spillover from subsurface to surface.

Supplementary Materials: The following supporting information can be downloaded at: <https://www.mdpi.com/article/10.3390/ma15227970/s1>, Figure S1: Total weight change during heating in air from 25 to 800 °C for the as-prepared samples produced by SCS using different fuels, additives and fuel-to-oxidizer ratios; Figure S2: XRD data for Ce–Fe oxide systems obtained by the SCS method using various types of fuel and fuel-to-oxidizer ratios; Figure S3: Dependence of the rate for a heterogeneous catalytic reaction on temperature; Table S1: Assignment of major absorption IR spectra peaks for the as-prepared samples produced by solution combustion synthesis using different fuels; Table S2 Data on the phase composition, crystallinity and reproducibility of the synthesized materials according to the refinement by the Rietveld method; Table S3: Influence of additions (glucose, NH₄NO₃) on glycine(or urea)-nitrate solution combustion process and the obtained SCS products; Table S4: The mass balance of combustion process; Table S5: Calculation of the volume of released CO₂ and time for its conversion.

Author Contributions: Conceptualization, A.N.M.; methodology, A.N.M. and S.O.O.; investigation, A.N.M., S.O.O. and M.A.G.; resources, D.A.S.; data curation, A.N.M.; writing—original draft preparation, A.N.M.; writing—review and editing, D.Y.M. All authors have read and agreed to the published version of the manuscript.

Funding: This research was funded by the Russian Science Foundation (grant number 22–23–20094, <https://rscf.ru/project/22-23-20094/>, accessed on 20 October 2022) and the St. Petersburg Science Foundation (agreement number 26/2022 from 14 April 2022).

Institutional Review Board Statement: Not applicable.

Informed Consent Statement: Not applicable.

Acknowledgments: The authors would like to thank research Maria Chebanenko (Ioffe Institute) and engineer Maria Serazhim (St. Petersburg State Institute of Technology (Technical University)) for performing two N₂ physisorption measurements.

Conflicts of Interest: The authors declare no conflict of interest.

References

1. Rodríguez-Padró, D.; Puente-Santiago, A.R.; Balu, A.M.; Muñ Oz-Batista, M.J.; Luque, R. Environmental Catalysis: Present and Future. *ChemCatChem* **2019**, *11*, 18–38. [[CrossRef](#)]
2. Dincer, I.; Acar, C. Review and Evaluation of Hydrogen Production Methods for Better Sustainability. *Int. J. Hydrogen Energy* **2015**, *40*, 11094–11111. [[CrossRef](#)]
3. Abe, J.O.; Popoola, A.P.I.; Ajenifuja, E.; Popoola, O.M. Hydrogen Energy, Economy and Storage: Review and Recommendation. *Int. J. Hydrogen Energy* **2019**, *44*, 15072–15086. [[CrossRef](#)]
4. Voorhoeve, R.J.H.; Johnson, D.W.; Remeika, J.P.; Gallagher, P.K. Perovskite Oxides: Materials Science in Catalysis. *Science* **1977**, *195*, 827–833. [[CrossRef](#)] [[PubMed](#)]
5. Monama, G.R.; Ramohlola, K.E.; Iwuoha, E.I.; Modibane, K.D. Progress on Perovskite Materials for Energy Application. *Results Chem.* **2022**, *4*, 100321. [[CrossRef](#)]
6. Yan, S.; Yim, C.-H.; Pankov, V.; Bauer, M.; Baranova, E.; Weck, A.; Merati, A.; Abu-Lebdeh, Y.; Gerbaldi, C. Perovskite Solid-State Electrolytes for Lithium Metal Batteries. *Batteries* **2021**, *7*, 75. [[CrossRef](#)]
7. Cao, Y.; Liang, J.; Li, X.; Yue, L.; Liu, Q.; Lu, S.; Asiri, A.M.; Hu, J.; Luo, Y.; Sun, X. Recent Advances in Perovskite Oxides as Electrode Materials for Supercapacitors. *Chem. Commun.* **2021**, *57*, 2343–2355. [[CrossRef](#)]
8. Xu, X.; Wang, Y.; Meng, H.; Zhu, T.; Yan, D.; Zhu, W.; Liu, S.; Zhao, Q. Perovskite-Perovskite Junctions for Optoelectronics: Fundamentals, Processing, and Applications. *Matter* **2022**, *5*, 2086–2118. [[CrossRef](#)]

9. Dang, T.T.; Nguyen, T.L.A.; Ansari, K.B.; Nguyen, V.H.; Binh, N.T.; Phan, T.T.N.; Pham, T.H.; Hang, D.T.T.; Amaniampong, P.N.; Kwao-Boateng, E.; et al. Perovskite Materials as Photocatalysts: Current Status and Future Perspectives. In *Nanostructured Photocatalysts: From Fundamental to Practical Applications*; Elsevier: Amsterdam, The Netherlands, 2021; pp. 169–216. [\[CrossRef\]](#)
10. Xu, X.; Pan, Y.; Ge, L.; Shao, Z. Perovskite Materials in Electrocatalysis. In *Revolution of Perovskite: Synthesis, Properties and Applications*; Arul, N.S., Nithya, V.D., Eds.; Springer: Singapore, 2020; pp. 209–250. ISBN 978-981-15-1267-4.
11. Roth, R.S. Classification of Perovskite and Other ABO_3 -Type Compounds. *J. Res. Natl. Bur. Stand.* **1957**, *58*, 75–88. [\[CrossRef\]](#)
12. Bhattar, S.; Abedin, M.A.; Kanitkar, S.; Spivey, J.J. A Review on Dry Reforming of Methane over Perovskite Derived Catalysts. *Catal Today* **2021**, *365*, 2–23. [\[CrossRef\]](#)
13. Joshi, A.; Shah, V.; Mohapatra, P.; Kumar, S.; Joshi, R.K.; Kathe, M.; Qin, L.; Tong, A.; Fan, L.S. Chemical Looping-A Perspective on the next-Gen Technology for Efficient Fossil Fuel Utilization. *Adv. Appl. Energy* **2021**, *3*, 100044. [\[CrossRef\]](#)
14. Goldschmidt, V.M. Die Gesetze Der Krystallochemie. *Naturwissenschaften* **1926**, *14*, 477–485. [\[CrossRef\]](#)
15. Galasso, F.S. Structure of Perovskite-Type Compounds. In *Structure, Properties and Preparation of Perovskite-Type Compounds*; Pergamon: Oxford, UK, 1969; pp. 3–49, ISBN 978-0-08-012744-6.
16. Park, N.G. Perovskite Solar Cells: An Emerging Photovoltaic Technology. *Mat. Today* **2015**, *18*, 65–72. [\[CrossRef\]](#)
17. Vyshatko, N.P.; Kharton, V.; Shaula, A.L.; Naumovich, E.N.; Marques, F.M.B. Structural Characterization of Mixed Conducting Perovskites $La(Ga,M)O_{3-\delta}$ (M = Mn, Fe, Co, Ni). *Mater. Res. Bull.* **2003**, *38*, 185–193. [\[CrossRef\]](#)
18. Richter, J.; Holtappels, P.; Graule, T.; Nakamura, T.; Gauckler, L.J. Materials Design for Perovskite SOFC Cathodes. *Mon. Chem.-Chem. Mon.* **2009**, *140*, 985–999. [\[CrossRef\]](#)
19. Fedorovskiy, A.E.; Drigo, N.A.; Nazeeruddin, M.K. The Role of Goldschmidt's Tolerance Factor in the Formation of A_2BX_6 Double Halide Perovskites and Its Optimal Range. *Small Methods* **2020**, *4*, 1900426. [\[CrossRef\]](#)
20. Inoue, I.H. Electrostatic Carrier Doping to Perovskite Transition-Metal Oxides. *Semicond. Sci. Technol.* **2005**, *20*, S112–S120. [\[CrossRef\]](#)
21. Zaboeva, E.A.; Izotova, S.G.; Popkov, V.I. Glycine-Nitrate Combustion Synthesis of $CeFeO_3$ -Based Nanocrystalline Powders. *Russ. J. Appl. Chem.* **2016**, *89*, 1228–1236. [\[CrossRef\]](#)
22. Choong, C.E.; Park, C.M.; Chang, Y.Y.; Yang, J.K.; Kim, J.R.; Oh, S.E.; Jeon, B.H.; Choi, E.H.; Yoon, Y.; Jang, M. Interfacial Coupling Perovskite $CeFeO_3$ on Layered Graphitic Carbon Nitride as a Multifunctional Z-Scheme Photocatalyst for Boosting Nitrogen Fixation and Organic Pollutants Demineralization. *Chem. Eng. J.* **2022**, *427*, 131406. [\[CrossRef\]](#)
23. Bertaut, F.; Forrat, F. Sur Les Déformations Dans Les Pérovskites à Base de Terres Rares et d'éléments de Transition Trivalents. *J. Phys. Radium* **1956**, *17*, 129–131. [\[CrossRef\]](#)
24. Petschnig, L.L.; Fuhrmann, G.; Schildhammer, D.; Tribus, M.; Schottenberger, H.; Huppertz, H. Solution Combustion Synthesis of $CeFeO_3$ under Ambient Atmosphere. *Ceram. Int.* **2016**, *42*, 4262–4267. [\[CrossRef\]](#)
25. Robbins, M.; Wertheim, G.K.; Mentsh, A.; Sherwood, R.C. Preparation and Properties of Polycrystalline Cerium Orthoferrite ($CeFeO_3$). *J. Phys. Chem. Solids* **1969**, *30*, 1823–1825. [\[CrossRef\]](#)
26. Kitayama, K.; Nojiri, K.; Sugihara, T.; Katsura, T. Phase Equilibria in the CeO and $CeFeO$ Systems. *J. Solid State Chem.* **1985**, *56*, 1–11. [\[CrossRef\]](#)
27. Ameta, J.; Kumar, A.; Ameta, R.; Sharma, V.K.; Ameta, S.C. Synthesis and Characterization of $CeFeO_3$ Photocatalyst Used in Photocatalytic Bleaching of Gentian Violet. *J. Iran. Chem. Soc.* **2009**, *6*, 293–299. [\[CrossRef\]](#)
28. Pandya, H.N.; Kulkarni, R.G.; Parsania, P.H. Study of Cerium Orthoferrite Prepared by Wet Chemical Method. *Mater. Res. Bull.* **1990**, *25*, 1073–1077. [\[CrossRef\]](#)
29. Selvam, K.; Jeeva, S.; Mani, G. Structural, Magnetic and Optical Properties of Cr Doped $CeFeO_3$ Nanoparticles Synthesized by Co-Precipitation Method. *JETIR* **2019**, *6*, 951–958.
30. Surendran, A.; Gupta, N.K.; Aziz, F.; Kushwaha, K.K. Synthesis and Characterization of Ce-Fe Composite Nanoparticles via Sol-Gel Method. *J. Nano-Electron. Phys.* **2020**, *12*, 01025. [\[CrossRef\]](#)
31. Opuchovic, O.; Kreiza, G.; Senvaitiene, J.; Kazlauskas, K.; Beganskiene, A.; Kareiva, A. Sol-Gel Synthesis, Characterization and Application of Selected Sub-Microsized Lanthanide (Ce, Pr, Nd, Tb) Ferrites. *Dye. Pigment.* **2015**, *118*, 176–182. [\[CrossRef\]](#)
32. Matveyeva, A.N.; Omarov, S.O.; Nashchekin, A.V.; Popkov, V.I.; Murzin, D.Y. Catalyst Supports Based on $ZnO-ZnAl_2O_4$ Nanocomposites with Enhanced Selectivity and Coking Resistance in Isobutane Dehydrogenation. *Dalton Trans.* **2022**, *51*, 12213–12224. [\[CrossRef\]](#)
33. Omarov, S.O.; Martinson, K.D.; Matveyeva, A.N.; Chebanenko, M.I.; Nevedomskiy, V.N.; Popkov, V.I. Renewable Hydrogen Production via Glycerol Steam Reforming over Ni/ CeO_2 Catalysts Obtained by Solution Combustion Method: The Effect of Ni Loading. *Fuel Process. Technol.* **2022**, *236*, 107429. [\[CrossRef\]](#)
34. Deganello, F.; Tyagi, A.K. Solution Combustion Synthesis, Energy and Environment: Best Parameters for Better Materials. *Prog. Cryst. Growth Charact. Mater.* **2018**, *64*, 23–61. [\[CrossRef\]](#)
35. Kingsley, J.J.; Patil, K.C. A Novel Combustion Process for the Synthesis of Fine Particle α -Alumina and Related Oxide Materials. *Mater. Lett.* **1988**, *6*, 427–432. [\[CrossRef\]](#)
36. Merzhanov, A.G.; Borovinskaya, I.P. Historical Retrospective of SHS: An Autoreview. *Int. J. Self-Propagating High-Temp. Synth.* **2008**, *17*, 242–265. [\[CrossRef\]](#)
37. Tang, P.; Zhang, J.; Fu, M.; Cao, F.; Lv, C. Characterization and Preparation Nanosized $CeFeO_3$ by a Microwave Process. *Integr. Ferroelectr.* **2013**, *146*, 99–104. [\[CrossRef\]](#)

38. Chen, X.; Chen, Y.; Song, C.; Ji, P.; Wang, N.; Wang, W.; Cui, L. Recent Advances in Supported Metal Catalysts and Oxide Catalysts for the Reverse Water-Gas Shift Reaction. *Front. Chem.* **2020**, *8*, 709. [[CrossRef](#)]
39. Zhu, M.; Ge, Q.; Zhu, X. Catalytic Reduction of CO₂ to CO via Reverse Water Gas Shift Reaction: Recent Advances in the Design of Active and Selective Supported Metal Catalysts. *Trans. Tianjin Univ.* **2021**, *26*, 172–187. [[CrossRef](#)]
40. González-Castaño, M.; Dorneanu, B.; Arellano-García, H. The Reverse Water Gas Shift Reaction: A Process Systems Engineering Perspective. *React. Chem. Eng.* **2021**, *6*, 954–976. [[CrossRef](#)]
41. Daza, Y.A.; Kuhn, J.N. CO₂ Conversion by Reverse Water Gas Shift Catalysis: Comparison of Catalysts, Mechanisms and Their Consequences for CO₂ Conversion to Liquid Fuels. *RSC Adv.* **2016**, *6*, 49675–49691. [[CrossRef](#)]
42. Jia, C.; Gao, J.; Dai, Y.; Zhang, J.; Yang, Y. The Thermodynamics Analysis and Experimental Validation for Complicated Systems in CO₂ Hydrogenation Process. *J. Energy Chem.* **2016**, *25*, 1027–1037. [[CrossRef](#)]
43. González-Cortés, S.L.; Imbert, F.E. Fundamentals, Properties and Applications of Solid Catalysts Prepared by Solution Combustion Synthesis (SCS). *Appl. Catal. A Gen.* **2013**, *452*, 117–131. [[CrossRef](#)]
44. Gheith, M.A. Differential Thermal Analysis of Certain Iron Oxides and Oxide Hydrates. *Am. J. Sci.* **1952**, *250*, 677–695. [[CrossRef](#)]
45. Tretyakov, Y.D.; Sorokin, V.V.; Kaul, A.R.; Erastova, A.P. Phase Equilibria and Thermodynamics of Coexisting Phases in Rare-Earth Element-Iron-Oxygen Systems. I. The Cerium-Iron-Oxygen System. *J. Solid State Chem.* **1976**, *18*, 253–261. [[CrossRef](#)]
46. Cam, T.S.; Vishnievskaya, T.A.; Popkov, V.I. Catalytic Oxidation of CO over CuO/CeO₂ Nanocomposites Synthesized via Solution Combustion Method: Effect of Fuels. *Rev. Adv. Mater. Sci.* **2020**, *59*, 131–143. [[CrossRef](#)]
47. Novitskaya, E.; Kelly, J.P.; Bhaduri, S.; Graeve, O.A. A Review of Solution Combustion Synthesis: An Analysis of Parameters Controlling Powder Characteristics. *Int. Mater. Rev.* **2021**, *66*, 188–214. [[CrossRef](#)]
48. Pourgolmohammad, B.; Masoudpanah, S.M.; Aboutalebi, M.R. Effects of the Fuel Type and Fuel Content on the Specific Surface Area and Magnetic Properties of Solution Combusted CoFe₂O₄ Nanoparticles. *Ceram. Int.* **2017**, *43*, 8262–8268. [[CrossRef](#)]
49. Varma, A.; Mukasyan, A.S.; Rogachev, A.S.; Manukyan, K.V. Solution Combustion Synthesis of Nanoscale Materials. *Chem. Rev.* **2016**, *116*, 14493–14586. [[CrossRef](#)] [[PubMed](#)]
50. Civera, A.; Pavese, M.; Saracco, G.; Specchia, V. Combustion Synthesis of Perovskite-Type Catalysts for Natural Gas Combustion. *Catal. Today* **2003**, *83*, 199–211. [[CrossRef](#)]
51. Galvita, V.V.; Poelman, H.; Bliznuk, V.; Detavernier, C.; Marin, G.B. CeO₂-Modified Fe₂O₃ for CO₂ Utilization via Chemical Looping. *Ind. Eng. Chem. Res.* **2013**, *52*, 8416–8426. [[CrossRef](#)]
52. Thommes, M.; Kaneko, K.; Neimark, A.V.; Olivier, J.P.; Rodriguez-Reinoso, F.; Rouquerol, J.; Sing, K.S.W. Physisorption of Gases, with Special Reference to the Evaluation of Surface Area and Pore Size Distribution (IUPAC Technical Report). *Pure Appl. Chem.* **2015**, *87*, 1051–1069. [[CrossRef](#)]
53. Liang, M.; Kang, W.; Xie, K. Comparison of Reduction Behavior of Fe₂O₃, ZnO and ZnFe₂O₄ by TPR Technique. *J. Nat. Gas Chem.* **2009**, *18*, 110–113. [[CrossRef](#)]
54. Wei, X.; Zhou, Y.; Li, Y.; Shen, W. Polymorphous Transformation of Rod-Shaped Iron Oxides and Their Catalytic Properties in Selective Reduction of NO by NH₃. *RSC Adv.* **2015**, *5*, 66141–66146. [[CrossRef](#)]
55. Saharuddin, T.S.; Samsuri, A.; Salleh, F.; Othaman, R.; Kassim, M.; Hisham, M.W.; Yarmo, M.A. The Reduction Behaviour of Cerium Doped Iron Oxide in Hydrogen and Carbon Monoxide Atmosphere. In *Materials Science Forum*; Trans Tech Publications Ltd.: Wallerau, Switzerland, 2016; Volume 840, pp. 381–385.
56. Perez-Alonso, F.J.; Melián-Cabrera, I.; López Granados, M.; Kapteijn, F.; Fierro, J.L.G. Synergy of Fe_xCe_{1-x}O₂ Mixed Oxides for N₂O Decomposition. *J. Catal.* **2006**, *239*, 340–346. [[CrossRef](#)]
57. Mutter, D.; Schierholz, R.; Urban, D.F.; Heuer, S.A.; Ohlerth, T.; Kungl, H.; Elsässer, C.; Eichel, R.-A. Defects and phase formation in non-stoichiometric LaFeO₃: A combined theoretical and experimental study. *Chem. Mater.* **2021**, *33*, 9473–9485. [[CrossRef](#)]
58. Mihai, O.; Chen, D.; Holmen, A. Chemical Looping Methane Partial Oxidation: The Effect of the Crystal Size and O Content of LaFeO₃. *J. Catal.* **2012**, *293*, 175–185. [[CrossRef](#)]
59. Faye, J.; Baylet, A.; Trentesaux, M.; Royer, S.; Dumeignil, F.; Duprez, D.; Valange, S.; Tatibouët, J.M. Influence of Lanthanum Stoichiometry in La_{1-x}FeO_{3-δ} Perovskites on Their Structure and Catalytic Performance in CH₄ Total Oxidation. *Appl. Catal. B Env.* **2012**, *126*, 134–143. [[CrossRef](#)]
60. Heidinger, B.; Royer, S.; Alamdari, H.; Giraudon, J.-M.; Lamonier, J.-F. Reactive Grinding Synthesis of LaBO₃ (B: Mn, Fe) Perovskite; Properties for Toluene Total Oxidation. *Catalysts* **2019**, *9*, 633. [[CrossRef](#)]
61. Qiao, D.; Lu, G.; Liu, X.; Guo, Y.; Wang, Y.; Guo, Y. Preparation of Ce_{1-2x}Fe_xO₂ Solid Solution and Its Catalytic Performance for Oxidation of CH₄ and CO. *J. Mat. Sci.* **2011**, *46*, 3500–3506. [[CrossRef](#)]
62. He, J.; Zhang, H.; Wang, W.; Yao, P.; Jiao, Y.; Wang, J.; Chen, Y. Soot Combustion over CeO₂ Catalyst: The Influence of Biodiesel Impurities (Na, K, Ca, P) on Surface Chemical Properties. *Environ. Sci. Pollut. Res.* **2021**, *28*, 26018–26029. [[CrossRef](#)]
63. Cheng, X.; Zhang, X.; Su, D.; Wang, Z.; Chang, J.; Ma, C. NO Reduction by CO over Copper Catalyst Supported on Mixed CeO₂ and Fe₂O₃: Catalyst Design and Activity Test. *Appl. Catal. B* **2018**, *239*, 485–501. [[CrossRef](#)]
64. Spencer, M.S. On the Activation Energies of the Forward and Reverse Water-Gas Shift Reaction. *Cat. Lett.* **1995**, *32*, 9–13. [[CrossRef](#)]
65. Landau, M.V.; Meiri, N.; Utsis, N.; Vidruk Nehemya, R.; Herskowitz, M. Conversion of CO₂, CO, and H₂ in CO₂ Hydrogenation to Fungible Liquid Fuels on Fe-Based Catalysts. *Ind. Eng. Chem. Res.* **2017**, *56*, 13334–13355. [[CrossRef](#)]

66. Utsis, N.; Vidruk-Nehemya, R.; Landau, M.V.; Herskowitz, M. Novel Bifunctional Catalysts Based on Crystalline Multi-Oxide Matrices Containing Iron Ions for CO₂ Hydrogenation to Liquid Fuels and Chemicals. *Faraday Discuss.* **2016**, *188*, 545–563. [[CrossRef](#)]
67. Li, S.; Ding, W.; Meitzner, G.D.; Iglesia, E. Spectroscopic and Transient Kinetic Studies of Site Requirements in Iron-Catalyzed Fischer–Tropsch Synthesis. *J. Phys. Chem. B* **2001**, *106*, 85–91. [[CrossRef](#)]
68. de Smit, E.; Weckhuysen, B.M. The Renaissance of Iron-Based Fischer–Tropsch Synthesis: On the Multifaceted Catalyst Deactivation Behaviour. *Chem. Soc. Rev.* **2008**, *37*, 2758–2781. [[CrossRef](#)]
69. Wezendonk, T.A.; Sun, X.; Dugulan, A.I.; van Hoof, A.J.F.; Hensen, E.J.M.; Kapteijn, F.; Gascon, J. Controlled Formation of Iron Carbides and Their Performance in Fischer–Tropsch Synthesis. *J. Catal.* **2018**, *362*, 106–117. [[CrossRef](#)]
70. Riedel, T.; Claeys, M.; Schulz, H.; Schaub, G.; Nam, S.S.; Jun, K.W.; Choi, M.J.; Kishan, G.; Lee, K.W. Comparative Study of Fischer–Tropsch Synthesis with H₂/CO and H₂/CO₂ Syngas Using Fe- and Co-Based Catalysts. *Appl. Catal. A Gen.* **1999**, *186*, 201–213. [[CrossRef](#)]
71. Landau, M.V.; Vidruk, R.; Herskowitz, M. Sustainable Production of Green Feed from Carbon Dioxide and Hydrogen. *ChemSusChem* **2014**, *7*, 785–794. [[CrossRef](#)]
72. Cui, X.; Xu, J.; Zhang, C.; Yang, Y.; Gao, P.; Wu, B.; Li, Y. Effect of Pretreatment on Precipitated Fe–Mo Fischer–Tropsch Catalysts: Morphology, Carburization, and Catalytic Performance. *J. Catal.* **2011**, *282*, 35–46. [[CrossRef](#)]
73. Ding, M.; Yang, Y.; Wu, B.; Wang, T.; Ma, L.; Xiang, H.; Li, Y. Transformation of Carbonaceous Species and Its Influence on Catalytic Performance for Iron-Based Fischer–Tropsch Synthesis Catalyst. *J. Mol. Catal. A Chem.* **2011**, *351*, 165–173. [[CrossRef](#)]
74. Liu, J.; Li, K.; Song, Y.; Song, C.; Guo, X. Selective Hydrogenation of CO₂ to Hydrocarbons: Effects of Fe₃O₄ Particle Size on Reduction, Carburization, and Catalytic Performance. *Energy Fuels* **2021**, *35*, 10703–10709. [[CrossRef](#)]
75. De la Rosa-Priego, F.A.; Gutierrez-López, E.D.; Zepeda, T.A.; Acosta-Alejandro, M.; Venezia, A.M.; Fuentes-Moyado, S.; Pawelec, B.; Noé Díaz-de-León, J. Enhanced CO₂ Hydrogenation to C₂₊ Hydrocarbons over Mesoporous X%Fe₂O₃–Al₂O₃ Catalysts. *Ind. Eng. Chem. Res.* **2021**, *60*, 18660–18671. [[CrossRef](#)]
76. Pérez-Alonso, F.J.; López Granados, M.; Ojeda, M.; Terreros, P.; Rojas, S.; Herranz, T.; Fierro, J.L.G.; Gracia, M.; Gancedo, J.R. Chemical Structures of Coprecipitated Fe–Ce Mixed Oxides. *Chem. Mater.* **2005**, *17*, 2329–2339. [[CrossRef](#)]
77. Pathak, L.C.; Singh, T.B.; Das, S.; Verma, A.K.; Ramachandrarao, P. Effect of PH on the Combustion Synthesis of Nano-Crystalline Alumina Powder. *Mater. Lett.* **2002**, *57*, 380–385. [[CrossRef](#)]
78. Lee, S.C.; Kim, J.S.; Shin, W.C.; Choi, M.J.; Choung, S.J. Catalyst Deactivation during Hydrogenation of Carbon Dioxide: Effect of Catalyst Position in the Packed Bed Reactor. *J. Mol. Catal. A Chem.* **2009**, *301*, 98–105. [[CrossRef](#)]
79. Albrecht, M.; Rodemerck, U.; Schneider, M.; Bröring, M.; Baabe, D.; Kondratenko, E.V. Unexpectedly Efficient CO₂ Hydrogenation to Higher Hydrocarbons over Non-Doped Fe₂O₃. *Appl. Catal. B* **2017**, *204*, 119–126. [[CrossRef](#)]
80. Zhang, J.; Wang, Y.; Tian, J.; Yan, B. Cu/LaFeO₃ as an Efficient and Stable Catalyst for CO₂ Reduction: Exploring Synergistic Effect between Cu and LaFeO₃. *AIChE J.* **2022**, *68*, e17640. [[CrossRef](#)]
81. Bahmanpour, A.M.; Héroguel, F.; Kılıç, M.; Baranowski, C.J.; Artiglia, L.; Röthlisberger, U.; Luterbacher, J.S.; Kröcher, O. Cu–Al Spinel as a Highly Active and Stable Catalyst for the Reverse Water Gas Shift Reaction. *ACS Catal.* **2019**, *9*, 6243–6251. [[CrossRef](#)]
82. Wei, G.; Zhou, H.; Huang, Z.; Zheng, A.; Zhao, K.; Lin, Y.; Chang, G.; Zhao, Z.; Li, H.; Fang, Y. Reaction Performance of Ce-Enhanced Hematite Oxygen Carrier in Chemical Looping Reforming of Biomass Pyrolyzed Gas Coupled with CO₂ Splitting. *Energy* **2021**, *215*, 119044. [[CrossRef](#)]
83. Li, K.; Haneda, M.; Ning, P.; Wang, H.; Ozawa, M. Microstructure and Oxygen Evolution of Fe–Ce Mixed Oxides by Redox Treatment. *Appl. Surf. Sci.* **2014**, *289*, 378–383. [[CrossRef](#)]
84. Goguet, A.; Meunier, F.C.; Tibiletti, D.; Breen, J.P.; Burch, R. Spectrokinetic Investigation of Reverse Water-Gas-Shift Reaction Intermediates over a Pt/CeO₂ Catalyst. *J. Phys. Chem. B* **2004**, *108*, 20240–20246. [[CrossRef](#)]
85. Ebrahimi, P.; Kumar, A.; Khraisheh, M. A Review of CeO₂ Supported Catalysts for CO₂ Reduction to CO through the Reverse Water Gas Shift Reaction. *Catalysts* **2022**, *12*, 1101. [[CrossRef](#)]
86. Chen, C.S.; Cheng, W.H.; Lin, S.S. Study of Iron-Promoted Cu/SiO₂ Catalyst on High Temperature Reverse Water Gas Shift Reaction. *Appl. Catal. A Gen.* **2004**, *257*, 97–106. [[CrossRef](#)]
87. Lin, L.; Yao, S.; Rui, N.; Han, L.; Zhang, F.; Gerlak, C.A.; Liu, Z.; Cen, J.; Song, L.; Senanayake, S.D.; et al. Conversion of CO₂ on a Highly Active and Stable Cu/FeO_x/CeO₂ Catalyst: Tuning Catalytic Performance by Oxide–Oxide Interactions. *Catal. Sci. Technol.* **2019**, *9*, 3735–3742. [[CrossRef](#)]